On-orbit Calibration and Performance of the EMIT Imaging Spectrometer

David R. Thompson[a], Robert O. Green[a], Christine Bradley[a], Philip G. Brodrick[a], Eyal Ben Dor[b], Matthew Bennett[a], Michael Bernas[a], Nimrod Carmon[a], K. Dana Chadwick[a], Roger N. Clark[c], Red Willow Coleman[a], Evan Cox[k], Ernesto Diaz[a], Michael L. Eastwood[a], Regina Eckert[a], Bethany Ehlmann[d], Paul Ginoux[e], María Gonçalves Ageitos[f,j], Kathleen Grant[h], Louis Guanter[i], Daniela Heller Pearlshtien[b], Mark Helmlinger[a], Harrison Herzog[a], Todd Hoefen[k], Yue Huang[l,m], Abigail Keebler[d], Olga Kalashnikova[a], Didier Keymeulen[a], Raymond Kokaly[k], Martina Klose[l], Longlei Li[o], Sarah Lundeen[a], Natalie Mahowald[o], John Meyer[k], Elizabeth Middleton[p], Ron L. Miller[m,n], Pantazis Mouroulis[a], Bogdan Oaida[a], Vicenzo Obiso[m], Francisco Ochoa[q], Winston Olson-Duvall[a], Gregory S. Okin[q], Thomas H. Painter[q,r], Carlos Pérez García-Pando[f,g], Vincent Realmuto[a], Lucas Shaw[a], Peter Sullivan[a], Erik Thingvold[a], Andrew K. Thorpe[a], Gregg Swayze[k], Suresh Vannan[a], Catalina Villarreal[a], Harold R. Pollock[s], Charlene Ung[a], Daniel W. Wilson[a], Sander Zandbergen[a]

[a] *Jet Propulsion Laboratory, California Institute of Technology, Pasadena, CA USA.*
[b] *Tel Aviv University, Tel Aviv, Israel.*
[c] *Planetary Science Institute, Tucson, AZ USA.*
[d] *California Institute of Technology, Pasadena, CA USA.*
[e] *Princeton University, Princeton, NJ USA.*
[f] *Barcelona Supercomputing Center, Barcelona, Spain.*
[g] *Catalan Institution for Research and Advanced Studies, ICREA, Barcelona, Spain.*
[h] *University of Southern California, Los Angeles, CA USA.*
[i] *Universitat Politècnica de València, Valencia, Spain.*
[j] *Universitat Politècnica de Catalunya, Barcelona, Spain.*
[k] *United States Geological Survey, Denver, CO USA.*
[l] *Karlsruhe Institute of Technology, Karlsruhe, Germany.*
[m] *NASA Goddard Institute for Space Studies, New York, NY USA.*
[n] *Columbia University, New York, NY USA.*
[o] *Cornell University, Ithaca, NY USA.*
[p] *NASA Goddard Space Flight Center, Greenbelt, MD USA.*
[q] *University of California Los Angeles, Los Angeles, CA USA.*
[r] *Airborne Snow Observatories, Inc., Mammoth Lakes, CA USA.*
[s] *Victoria University of Wellington, Wellington, New Zealand*

Abstract

The Earth surface Mineral dust source InvesTigation (EMIT) is a remote visible to shortwave infrared (VSWIR) imaging spectrometer that will map the mineralogy of Earth's mineral dust forming regions. EMIT was launched to the International Space Station in July 2022, beginning a year-long mission. This article describes the EMIT spectroradiometric calibration and on-orbit validation experiments. EMIT achieves several notable firsts for an instrument of its class. It demonstrates successful on-orbit adjustments of Focal Plane Array (FPA) alignment with sub-micron precision. It offers spectral uniformity better than 98%. Optical artifacts in the measurement channels are at least three orders of magnitude below the primary signal. EMIT consists of just six optical elements, no shutter, and no onboard calibration systems. With this simple and efficient design, EMIT satisfies the stringent needs for the next generation of VSWIR imaging spectrometers.

1. Introduction

The Visible to Shortwave Infrared (VSWIR) spectral range is sensitive to diverse Earth surface properties making it useful for a wide range of remote sensing applications. Imaging spectrometers, also known as hyperspectral imagers, acquire rasters of spectra to map geophysical phenomena. The first imaging spectrometers were developed over 40 years ago (Goetz & Srivastava, 1985), but they have recently reached a new stage of maturity with orbital instruments conducting global investigations. These missions include DESIS (Alonso et al., 2019), PRISMA (Cogliati et al., 2021), HiSUI (Matsunaga et al., 2020), and EnMAP (Guanter et al., 2015; Chabrillat et al., 2020). Upcoming missions like CHIME (Nieke & Rast, 2018) and the Surface Biology and Geology (SBG) investigation (Cawse-Nicholson et al., 2021) are anticipated to provide regular coverage of Earth's entire land area and coastal waters. Simultaneously, advances in computing enable more sophisticated algorithmic analyses, portending a new era of spectroscopic remote sensing.

State of the art spectroscopic analyses require accurate calibration. Even when the Earth's surface reflectance is spectrally smooth, atmospheric absorption features are sharp. This makes geophysical retrievals sensitive to wavelength miscalibrations at the sub-nanometer level (Thompson et al., 2021). Atmospheric errors often exceed instrument noise as a contribution to measurement uncertainty, and can introduce atmosphere-dependent errors leading to regional biases in global maps (Carmon et al., 2020). Precise knowledge of each channel's spectral response function is critical to preserve atmospheric absorption shapes. Moreover, high radiometric accuracy is needed to remove atmospheric distortions by Rayleigh scattering. High unifor-

Figure 1: EMIT deployed to the ISS. EMIT is the white box mounted at the lower left on the ELC1 rack at the top of the image. Credit: NASA.

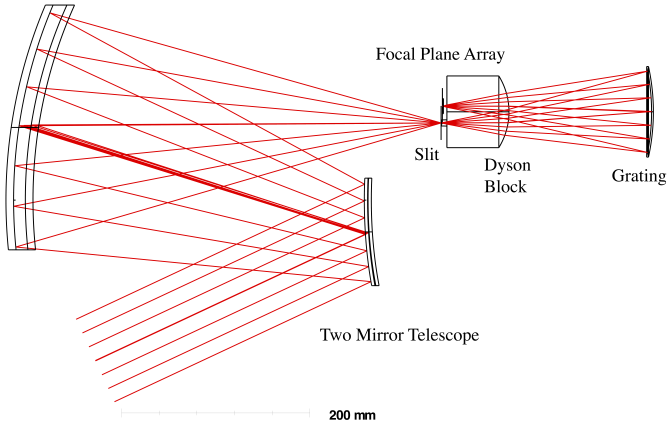

Figure 2: EMIT optical layout. Red lines illustrate light pathways, and instrument components are in black. A two-mirror telescope images incoming light onto a slit that limits the field of view to a line across the Earth's surface. Light then passes through the Dyson lens, is spectrally dispersed by the grating, travels back through the same Dyson lens, and finally intersects the focal plane array detector.

mity of both radiometric and spectral calibration is needed for consistent surface property measurements throughout the instrument field of view. In these and other ways, the performance of remote spectroscopy is often limited by systematic calibration uncertainty rather than instrument noise. Improving spectroradiometric accuracy will be critical to fulfill the promise of future missions.

This paper describes the on-orbit calibration and validation of the Earth surface Mineral dust source InvesTigation (EMIT), a VSWIR imaging spectrometer with high spectroradiometric performance. EMIT was sponsored by the National Aeronautics and Space Administration (NASA) and developed at the Jet Propulsion Laboratory (Green et al., 2018, 2020). It is now installed on the International Space Station (ISS, Figure 1), where it is mapping the mineralogy of Earth's mineral dust forming regions. These measurements will constrain the composition of the emitted dust, enabling Earth System Models to predict the capacity of these particles to absorb solar radiation, along with the associated radiative forcing and climate response (Green et al., 2020; Connelly et al., 2021; Li et al., 2021). The EMIT Instrument launched to the ISS on July 14, 2022 and was installed on the port side of the truss structure in the ExPReSS Logistics Carrier-1 (ELC1) rack (Cook, 2004). It measured first light on July 28 and began

Parameter	**Requirement**	**As measured**
Spectral range	410 - 2450 nm	380 - 2500 nm
Spectral sampling	< 10 nm	< 7.5 nm
Spatial sampling	30-80 m	≈ 60 m
Swath width	> 1200 elements	> 1240 elements
Spectral response (FWHM)	< 13 nm	< 8.5 nm
Channel wavelength uniformity	> 90%	> 98%
FWHM uniformity	n/a	> 98%
Signal to Noise Ratio (SNR)	> 190 at 700 nm	> 500 at 700 nm
Stray spectral/spatial response	< 0.002	< 0.0001 corrected
Dark current drift	n/a	< 1 DN / 12 hours

Table 1: EMIT Performance. SNR requirements are defined relative to a stressing case observation at 45 degrees solar zenith with a 20% surface reflectance. SNR requirements at other wavelengths are exceeded by a similar factor. We show the stray spectral response requirement for the region 5-81 channels from center, relative to peak response.

conducting on-orbit checkout procedures. At the time of this writing, EMIT has acquired thousands of scenes globally.

Table 1 lists the key mission performance requirements derived from the mineral dust objectives. For example, EMIT must measure the full VSWIR range to capture minerals' electronic absorptions in the visible range and vibrational overtones in the shortwave infrared. The spatial sampling must be fine enough to map soils in fallow farm fields. Radiometric precision should be sufficient to identify a 2% change in the hematite absorption feature, a difference which, if it appeared throughout North Africa, could change the net contribution of global dust-related atmospheric forcing from heating to cooling or vice versa. The spectral calibration should be spatially uniform within 10% to facilitate atmospheric correction and identification of mineral species in the shortwave infrared. Table 1 constitutes a challenging set of performance objectives that must be confirmed on-orbit along with the calibration.

To achieve this performance, EMIT adopts the Compact Wide Swath Imaging Spectrometer design of Van Gorp et al. (2016). It has a simple optical layout (Bradley et al., 2020) with a two mirror aluminum telescope and a Dyson imaging spectrometer (Figure 2). The spectrometer uses a calcium fluoride lens and a custom-fabricated grating produced by the Jet Propulsion Laboratory Microdevices Laboratory (Mouroulis et al., 1998). It covers the 380-2500 nm range at approximately 7.5 nm sampling. Its detector is a 480x1280-format cryogenic Mercury Cadmium Telluride array from Teledyne Technologies Inc., of similar design to their CHROMA series (Sullivan et al., 2017). During operation, 328 channels of this array are used. EMIT also carries a flight electronics suite: the Focal Plane Interface Electronics-Analog (FPIE-A), which digitizes signals from the FPA; and the Focal Plane Interface Electronics-Digital (FPIE-D), a high performance embeded computing system (Keymeulen et al., 2022) that processes the data, and applies onboard cloud screening and compression to reduce data volumes. Unlike contemporary instruments of its class, EMIT carries no onboard shutter or calibration mechanism. Its simple design emphasizes spectral fidelity and radiometric stability to enable on-orbit calibration with vicarious targets.

This manuscript reports EMIT's post-launch calibration and performance assessment. It documents our methods and quantifies data product accuracy. We focus here on the spectral and radiometric characteristics which are central to EMIT's science objectives. Section 2 discusses spectral calibration, which measures the sensitivity of each Focal Plane Array (FPA) element to different wavelengths. This includes the center wavelength position, the spectral response function, and corrections for stray spectral response. Section 3 describes radiometric calibration, which translates instrument digital numbers to units

of radiance. We describe corrections for optical ghosts, measurement and validation of radiometric calibration coefficients, measurement of spatial nonuniformities, and corrections for bad FPA elements. We then evaluate radiometric performance over several field sites where ground truth reflectance data are available. Section 4 concludes with the implications for EMIT science and future missions. EMIT shows the spectral and radiometric accuracy now achievable by contemporary instruments, an example that can inform future missions like ESA's CHIME and NASA's SBG.

For reproducibility, all code and data for these experiments are available from public archives. The radiometric calibration code and files are available from the public EMIT mission repository (Olson-Duvall et al., 2022). EMIT mission data is available at the NASA's Land Processes Distributed Active Archive Center (LP DAAC) (Green et al., 2022). EMIT also produces a range of derived data products, including surface reflectance, mineral maps, and Earth system model runs. We focus here on the initial calibration, but still use atmospheric radiative transfer models in several experiments. Code to configure and run these models is available from the ISOFIT repository (Thompson et al., 2019b). In situ field data is available from the United States Geological Survey (USGS) (Meyer et al., 2023b,a).

2. Spectral calibration

Imaging spectrometers view the Earth through a range of sharp atmospheric absorption features. Analysts model these absorptions to infer the underlying surface reflectance signal (Figure 3). The instrument spectral resolution is coarser than the atmospheric features, so the center wavelength and spectral response of each channel must be known with high accuracy. This mapping must be uniform in the spatial dimension. Any nonuniformities, such as spectral smile or tilt, force the analyst to either resample the spectra or model cross-track elements independently. Even these measures cannot correct nonuniformities completely, making spectral uniformity a critical performance parameter (Thompson et al., 2021). The following subsections describe our procedure for measuring wavelength center calibrations and spectral response functions, and for quantifying EMIT uniformity.

2.1. Channel center wavelength calibration

The EMIT channel spacing, also known as the *dispersion*, varies slightly with wavelength and must be determined from instrument data. We begin with laboratory measurements, coupling five lasers at known wavelengths into an integrating sphere. A scan mirror in the EMIT vacuum chamber translates this stimulus across the EMIT field of view. We fit a *dispersion curve*, representing channel spacing as a function of wavelength, to the laser stimulus at all spatial positions. We initialize the dispersion curve with EMIT optical models (Bradley et al., 2020). We then optimize an additive offset and multiplicative stretch to the plot of dispersion vs. wavelength, finding the values which best predict the observed laser lines using a least squares approach.

The laboratory data are limited by the number and wavelength stability of the lasers, so we revise them after launch using features of the Earth's atmosphere. Unique infrared spectral absorptions, such as water vapor and oxygen, reveal wavelength calibration (Guanter et al., 2007; Thompson et al., 2015b; Kuhlmann et al., 2016). Specifically, we optimize a wavelength shift to fit the modeled absorption features to the measured radiance. Fitting the spectrum well requires estimating other parameters of the Earth's atmosphere and surface. For example, the underlying surface reflectance varies as a function of wavelength, with overlapping features that if unmodeled could shift the apparent positions or shapes of atmospheric features (Gao et al., 1993). Moreover, atmospheric water vapor varies spatially and temporally. Such free parameters must be optimized simultaneously.

Here, we obtain a simultaneous *maximum a posteriori* estimate of surface, atmosphere, and instrument parameters following Thompson et al. (2018b). We fit a state vector $\mathbf{x}$ which includes: the surface reflectance in each instrument channel; the atmospheric water vapor concentration in g cm^{-2}; the change in wavelength position versus the original calibration; and the change in the Full Width at Half Maximum (FWHM) of the spectral response functions. We represent the wavelength shift as a function of channel number with a four-knot cubic spline. We place knots at the extrema and at channels 520 and 1790 nm, where our optical models imply inflections in the second derivative of wavelength dispersion. The instrument spectral response is a single parameter representing a spectrally-uniform growth or contraction of the FWHMs relative to the laboratory estimates.

We relate the state vector $\mathbf{x}$ to the radiance measurement $\mathbf{y}$ using a forward model $\mathbf{F}(\mathbf{x})$ and random noise ϵ such that:

$$\mathbf{y} = \mathbf{F}(\mathbf{x}) + \epsilon \tag{1}$$

The forward model describes the radiance measurement at the sensor for any hemispherical directional surface reflectance spectrum $\rho_\mathbf{s}$ using the following expression (Vermote et al., 1997):

$$\mathbf{L}_{obs} = \mathbf{F}(\mathbf{x}) = \mathbf{L_a} + \frac{\mathbf{L}_\downarrow}{\mathbf{1} - \mathbf{s} \circ \boldsymbol{\rho}_\mathbf{b}} \circ \left[\mathbf{t}^\uparrow_\mathbf{dir} \circ \boldsymbol{\rho}_\mathbf{s} + \mathbf{t}^\uparrow_\mathbf{dif} \circ \boldsymbol{\rho}_\mathbf{b}\right] \tag{2}$$

where $\circ$ is element-wise multiplication and the vinculum is element-wise division. Here $\mathbf{L}_{obs}$ is the radiance at aperture. The symbol $\boldsymbol{\rho}_b$ represents the average reflectance of the terrain outside the pixel. For the large playa surfaces in the experiments that follow, we assume $\boldsymbol{\rho}_s$ and $\boldsymbol{\rho}_b$ are equal. The other terms are optical coefficients calculated using the MODTRAN radiative transfer model version 6.0 (Berk et al., 2014). We configure MODTRAN using the observing geometry, solar geometry, and atmospheric state, producing the upward direct beam transmittance $\mathbf{t}^\uparrow_\mathbf{dir}$, the upward diffuse transmittance $\mathbf{t}^\uparrow_\mathbf{dif}$, the spherical sky albedo at the bottom of the atmosphere $\mathbf{s}$, the path radiance $\mathbf{L_a}$, and the downwelling radiance $\mathbf{L}_\downarrow$ from a target with reflectance unity at the bottom of the atmosphere. We use the Fontenla et al. (2011) model for solar irradiance. We run the radiative transfer model over a grid of atmospheric state values, filling a multidimensional lookup table that can be interpolated at runtime to find the atmospheric optical coefficients for any state vector $\mathbf{x}$.

The best estimate of $\mathbf{x}$ is that with the highest *a posteriori* probability, accounting for both the measurement and prior knowledge about probable state vector configurations. We find this $\mathbf{x}$ by minimizing the following equivalent cost function (Thompson et al., 2018b):

$$\chi(\mathbf{x}) = (\mathbf{F}(\mathbf{x}) - \mathbf{y})^\mathbf{T}\mathbf{S}_\epsilon^{-1}(\mathbf{F}(\mathbf{x}) - \mathbf{y}) \; + (\mathbf{x} - \mathbf{x_a})^\mathbf{T}\mathbf{S}_\mathbf{a}^{-1}(\mathbf{x} - \mathbf{x_a}) \tag{3}$$

The symbol $\mathbf{S}_\epsilon$ is the covariance of the zero mean observation noise ϵ. This term penalizes departure of the modeled radiance from the measurement, accounting for the observation noise covariance. For typical instrument performance with signal to noise ratios (SNRs) in the hundreds, the solution is insensitive to noise magnitude. Consequently, for these tests we used a diagonal covariance noise matrix with a conservative spectrally-uniform SNR of 200. In later sections, we construct a more accurate noise model.

The second term of equation 3 penalizes departure of the state vector from the prior distribution. Here the prior is a multivariate Gaussian with mean $\mathbf{x_a}$ and covariance $\mathbf{S_a}$. The atmospheric elements are independent from each other and from the surface reflectance elements.

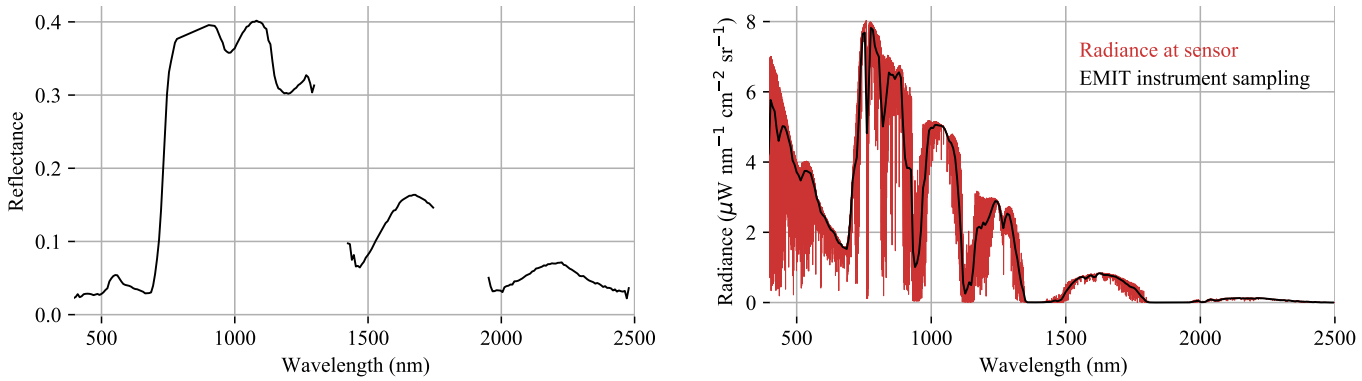

Figure 3: Accurate estimation of surface reflectance requires accurate spectral calibration. The left panel shows an EMIT measured reflectance spectrum from a forest in Manchuria (scene ID emit20220820t035232). The right panel shows its simulated radiance spectrum at high resolution (red) and EMIT instrument sampling (black). Removing atmospheric effects requires modeling the instrument's sampling of these sharp atmospheric features.

The surface reflectance elements are correlated via a block diagonal covariance matrix that aims to capture the actual statistics of physical surface reflectance spectra. We select this prior from a set of multivariate Gaussian distributions as in Thompson et al. (2018b). We fit these distributions using a library of terrestrial spectra from the USGS Spectral library (Kokaly et al., 2017), and other community libraries (Herold et al., 2004; Dennison & Gardner, 2000; Thompson et al., 2019a), all of which had been manually cleaned of artifacts, curated and uploaded as EMIT mission libraries to the Ecological Spectral Information System (ECOSIS) spectral catalog (Wagner et al., 2018). At runtime, we calculate an initial guess of surface reflectance using a band ratio retrieval of water vapor as in Schläpfer et al. (1998). We then find the Euclidean-nearest Gaussian component to serve as the prior. This enables the retrieval to account for the unique reflectance statistics of vegetation and snow, which have overlapping absorptions in the near infrared range, producing consistent wavelength fit over heterogeneous terrain. To avoid biasing the reflectance magnitude, all prior means and covariances are rescaled to match the Euclidean norm of the initial guess as in Thompson et al. (2018b).

We update the dispersion curve using a scene in North Africa (scene ID emit20220814t145733) with a clear flat surface. We average the data cube in the downtrack direction, reducing the image to a single row. We then fit the wavelength spline function independently to each spectrum, together with surface reflectance and atmospheric state variables. Departing from EMIT's operational atmospheric correction, we use a dense prior covariance which models cross-correlations between surface reflectance in all wavelengths from 380 to 2500 nm. This enforces reflectance smoothness in all channels so that atmospheric absorption features can constrain the instrument dispersion across the full VSWIR interval. The resulting wavelength dispersion curve appears in Figure 4. The pre-launch and post-launch wavelength calibration is nearly identical at 500 nm. The discrepancy peaks at about -0.35 nm, about 2% of a channel width, near 1900 nm. We find no significant change in spectral response functions. The measured sampling of < 7.5 nm and FWHM of 8.5 nm significantly outperform mission requirements of 10 nm and 13 nm, respectively (Table 1).

2.2. *Channel center wavelength uniformity*

We next assessed the spatial nonuniformity of the wavelength/channel assignments. As before, this process begins in the laboratory with the laser integrating sphere, by measuring the laser centroid at each cross-track location. Figure 5 shows the result for one of the more accurate lasers, at 1949 nm. A slight ripple in the measurement could be instability in the laser or other uncertainty in ground support equipment. The laser line centroids are consistent to within approximately 0.2 nm at all spatial positions, a uniformity of 98% in pixel units relative to a requirement of 90% (Table 1). A linear fit shown in red has no measurable slope, consistent with a properly-clocked FPA.

As in the dispersion fits, the state vector for spatial uniformity includes parameters for both center wavelength and spectral response functions. The center wavelength parameterization differs slightly; instead of a multiparameter dispersion spline, we fit a single additive offset that shifts the wavelength axis horizontally. We fit this offset independently at each cross-track location, along with the surface and atmosphere terms. This parameterization has an advantage that it can be performed on a subset of the spectrum, facilitating repeat tests on multiple, distinct atmospheric features. Figure 6 shows wavelength center channel deviation as a function of cross track position, estimated using the interval from 785 to 1250 nm which contains multiple water vapor absorptions. Independent fits of the oxygen A band absorption at 760 nm yield a similar answer, improving confidence in the result. The measurement standard error for a single pixel is on the order of one percent of a channel width. After launch, EMIT shows about 0.15 nm of spectral smile. This is visible as a parabolic deviation in the wavelength center position. There is also an additional 0.1 nm of tilt, visible as a slope in the red best-fitting line.

EMIT can dynamically adjust its FPA position by changing the temperature of the mounting components. We used pre-launch tests to develop a thermomechanical model relating the component temperatures to the FPA position. We used this model to determine a temperature change that would remove the tilt. On August 13 2022 we commanded the new setpoint, and then re-measured the tilt in a new scene (ID emit20220813t215020). We find that the initial tilt has been removed (Figure 7) and the slope is no longer measurable. A subsequent test in January 2023 repeated the demonstration, when, after an instrument thermal cycle, the FPA showed a smaller tilt in the opposite direction. This tilt was also corrected to within our measurement precision. These tests demonstrate positional control on the order of 200 nm for an instrument of 300 mm in size. To our knowledge, this is the first demonstration of on-orbit FPA mechanical adjustments by an imaging spectrometer in flight, and the most spatially-uniform alignment yet achieved for an instrument of this class. The center-to-peak shift of about 0.1 nm satisfies the most stressing measurement needs of future global spectrometers like SBG (Thompson et al., 2021).

2.3. *Spectral response functions*

In addition to the wavelength center position, we characterize the spectral response function of each channel. This is typically taken to be Gaussian and constant across all spatial positions, but slight deviations are inevitable. To assess this parameter we first measure the pre-launch response functions in the laboratory. A monochromator sweeps a spectrally-narrow stimulus across all wavelengths in sequence. The rise and fall of this signal at a given channel indicates the widths of its Full Width at Half Maximum (FWHM).

We re-measure the spectral response functions after launch using the procedures outlined in Section 2.1, with a single parameter that expands or shrinks the FWHM at all channels. We do not find any significant differences beyond the original laboratory calibration, but when we perform this fit at all spatial positions, a small but measurable spatial nonuniformity appears. Figure 8 shows a symmetric "w" curve in FWHM as a function of spatial position. This feature is consistent with laboratory data. The standard deviation of 0.16 nm is less than 2% of the FWHM, a level which is unlikely to be noticeable during most EMIT investigations. Consequently, EMIT processing uses a single spectral response function for each channel regardless of spatial position, an approximation which significantly simplifies science data processing.

2.4. *Stray spectral response*

The last spectral calibration activity measures non-Gaussian components of the spectral response function. Real instrument spectral response is non-Gaussian due to scatter from the grating and other optical elements in the spectrometer. In particular, the tails of the response function are slightly super-Gaussian. In the worst case this could cause distortions such as blurring of the spectrum and inaccurate retrieval of atmospheric parameters (Thompson et al., 2018a). The response of a single pixel is similar to the FPA image of a bright single-pixel source. This fact enables a laboratory measurement based on spatial filters and a monochromator to supply a sub-channel source. We then average a large number of frames to reduce noise and resolve the faint tail structure. We model the extra response with a set of concentric Gaussians. The model at position p uses the following form:

$$R(p,\mu,\zeta_1,\zeta_2,\zeta_3,\sigma_1,\sigma_2,\sigma_3) = \zeta_1 e^{-0.5(p-\mu)^2/\sigma_1^2} + \zeta_2 e^{-0.5(p-\mu)^2/\sigma_2^2} + \zeta_3 e^{-0.5(p-\mu)^2/\sigma_3^2} \quad (4)$$

where μ is the center position of the stimulus, σ_1 is the standard deviation of the central peak, and σ_2 and σ_3 are the standard deviations

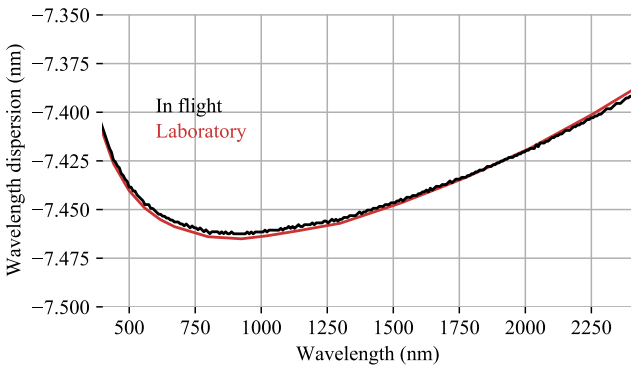

Figure 4: EMIT Wavelength dispersion resulting from on-orbit and laboratory measurements.

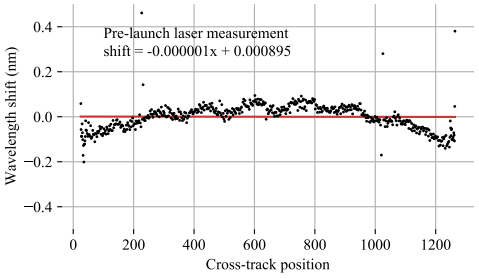

Figure 5: EMIT FPA clocking before launch, as measured at 1949 nm with a laser source. We report the shift as a linear trend in nm per pixel, plotted as a red line.

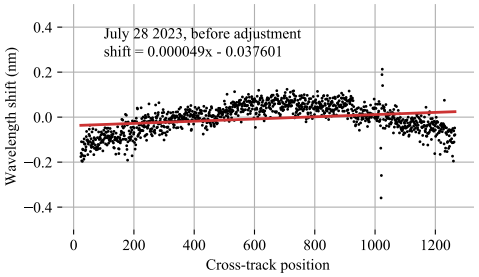

Figure 6: EMIT FPA clocking after launch, as measured with atmospheric water vapor from 800-1200 nm. We report the shift as a linear trend in nm per pixel, plotted as a red line.

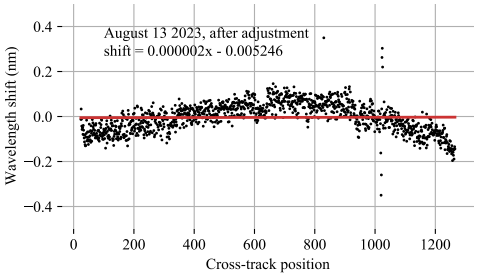

Figure 7: EMIT on-orbit FPA clocking update, as measured with atmospheric water vapor. We report the shift as a linear trend in nm per pixel, plotted as a red line.

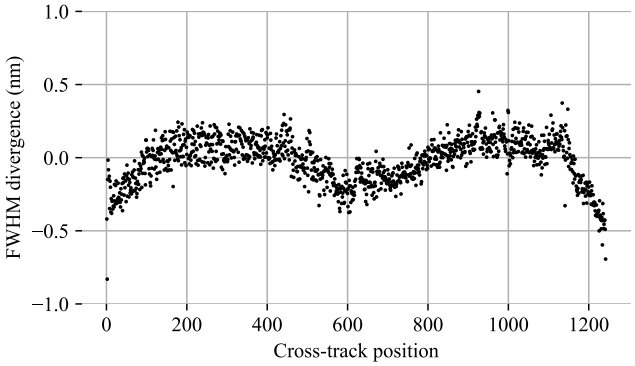

Figure 8: Cross track deviation of SRFs, as measured with atmospheric water vapor (scene ID emit20220813t215020).

of the Gaussians forming the stray spectral response. The ζ terms are scaling coefficients on the Gaussian magnitudes. We fit free parameters to match the response function in logarithmic coordinates, with the cost function:

$$c(\mu, \zeta_1, \zeta_2, \zeta_3, \sigma_1, \sigma_2, \sigma_3) = \sum_{p \in \mathcal{P}} [\log(x(p)) - \log(R(p, \mu, \zeta_1, \zeta_2, \zeta_3, \sigma_1, \sigma_2, \sigma_3))]^2 \quad (5)$$

We fit these functions in both the spatial and spectral dimensions, scanning across all spectral channels $\mathcal{P}$ at a single field point.

Next, having measured these response functions at each FPA location, we develop a correction based on the linear deconvolution process of Zong et al. (2006), revisited in Brachmann et al. (2016) and Thompson et al. (2018a). This treats the stray spectral response function as an operator which convolves an additional blurring kernel on the original spectrum. We represent the blur as a matrix operator, with rows containing the stray spectral response. This operator multiplies the original spectrum to produce the additional blur. We define the measured radiance spectrum $\mathbf{L}_{obs}$ as a vector with dimensionality equal to the number of instrument channels n, the ideal radiance $\mathbf{L}_N$ as a vector representing the measurement in the absence of stray spectral response, and the true high spectral resolution radiance at aperture $\mathbf{L}_a$ with dimensionality m much greater than the number of instrument channels. We also define two sampling operators, a nominal Gaussian response matrix $\mathbf{H}$ of size $n \times m$, and a stray spectral response function matrix $\mathbf{G}$ of size $n \times n$, with spectral response functions on the rows of the matrix. We have:

$$\begin{aligned} \mathbf{L}_{obs} &= \mathbf{GHL}_A + \mathbf{HL}_A + \epsilon \\ \mathbf{L}_{obs} &= \mathbf{GL}_N + \mathbf{L}_N + \epsilon \\ &= [\mathbf{G} + \mathbf{I}]\mathbf{L}_N + \epsilon \\ &= \mathbf{AL}_N + \epsilon \end{aligned} \quad (6)$$

The matrix $\mathbf{A}$ contains stray spectral response functions (SSRFs) measured in the laboratory, with one added to the diagonal elements (Zong et al., 2006). To estimate the ideal channelized radiance from a blurred measurement we take the Moore-Penrose pseudoinverse $\mathbf{A}^+ = (\mathbf{A}^T\mathbf{A})^{-1}\mathbf{A}^T$ which enforces $\mathbf{A}^+\mathbf{A} = \mathbf{I}$. We multiply this correction operator with the original vector:

$$\hat{\mathbf{L}}_{obs} = \mathbf{A}^+\mathbf{L}_M \quad (7)$$

We perform this procedure independently in spatial and spectral dimensions, resulting in two matrix operators applied independently at runtime to correct the EMIT data.

Figure 9 shows an example. The top panel shows spectral correction of a laboratory monochromatic source held out of the fitting procedure. The original response appears in red. Our correction recovers the ideal Gaussian response, a parabola in logarithmic coordinates (in black). The bottom panel shows the spatial correction. Even without software correction, deviations from Gaussianity are almost three orders of magnitude below the peak, outperforming mission requirements for stray response (Table 1). It is considerably better than many historical grating-based instruments like AVIRIS-NG (Thompson et al., 2018a). We attribute this improvement to a new grating designed explicitly to reduce scatter. After the software correction, deviations are no longer measurable in laboratory data.

Validating the improvement on remote reflectance retrievals is more challenging, since the magnitude of the correction for EMIT is small and the differences are easily masked by changes to the retrieved atmospheric state. We look to the water vapor feature at 1800-1900 nm,

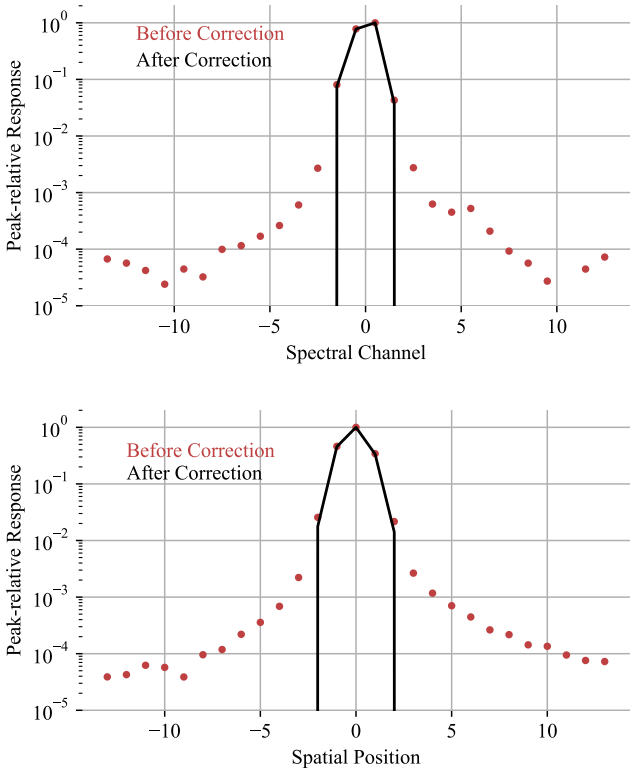

Figure 9: EMIT spectral response function (top) and spatial response function (bottom), before and after correction for stray response.

where absorption is so strong that the lower troposphere is effectively opaque to remote instruments. These radiance channels should contain only noise that is decorrelated from the surface reflectance signal. Any visible evidence of surface features in these channels represents unwanted spectral scatter from neighboring bands. To assess this effect, we extracted a rectangular region approximately 20x20 km from an arid-land scene, with high-contrast features that showed a range of surface albedos (scene ID emit20220807t183301). The image of the absorbed channel at 1841 nm showed some weak evidence of features from the surface at a level close to the noise. The correlation coefficient with the neighboring unabsorbed channel at 1744 nm was 0.29. After the SSRF correction, surface features were nearly imperceptible and the correlation coefficient dropped to just 0.13, evidence that the spectral response correction was achieving the desired effect.

3. Radiometric calibration

EMIT's radiometric calibration maps the intensity of the sensor response, expressed in instrument digital numbers, to radiance at aperture in units of μW nm^{-1} cm^{-1} sr^{-1}. Figure 10 shows the steps in the procedure. Radiometric calibration also requires replacing nonfunctional detector elements in the FPA and correcting any optical artifacts such as ghosts. We discuss each of these operations in the sections that follow.

We use a linear model of the observed radiance L_{obs} with a zero point d_0, gain factors ν, and digital number measurement d. The radiance is a function of FPA row r and column c:

$$L_{obs}(r, c) = \nu(r, c)\,[d(r, c) - d_0(r, c)] \quad (8)$$

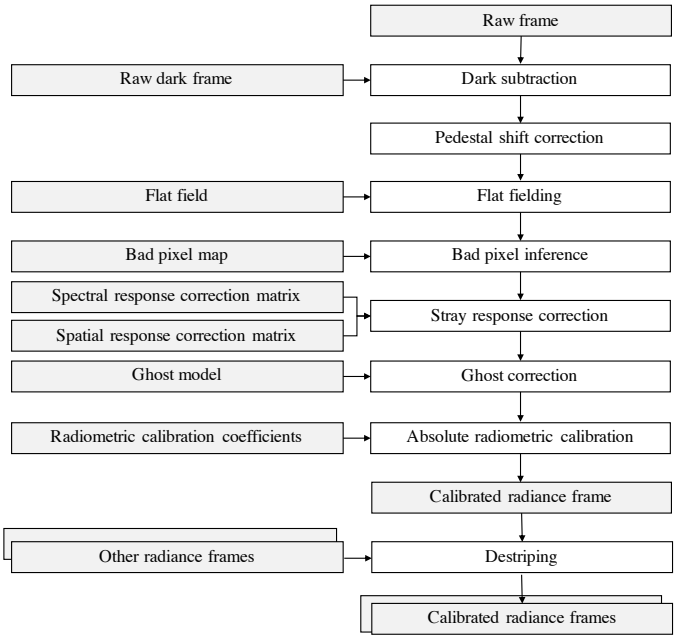

Figure 10: Radiometric calibration procedure. Grey boxes correspond to data inputs, white boxes to procedures.

The gain factors ν can be further decomposed into radiometric calibration coefficients, one per channel, and a flat field image representing spatial nonuniformities in radiometric response. In practice the response is nonlinear due to limitations of the detector and amplifier circuits. Measuring these nonlinearities requires accurate knowledge of relative illumination. Conventional methods, such as changing integration times, photodiode standards, or blocking meshes, often have systematic errors as large as the signal being measured. For this reason, and because the detector and amplifiers are already nearly linear by design, we do not apply any linearity corrections to the data.

3.1. Zero point estimation

The first step of the calibration finds the zero point for each FPA element. The zero point is the Digital Number (DN) corresponding to zero illumination. It changes on different timescales due to varied effects such as the thermal dark current and electronic phenomena. We measure long-timescale changes with an image of a dark scene from the same orbit as each EMIT science image. We take the temporal median of dark frames to find a dark measurement d_k. The dark-subtracted frame is:

$$d_{ds} = d - d_k \tag{9}$$

The EMIT instrument has no shutter, so we acquire dark frames over the non-sunlit side of the Earth. It is important that these scenes be truly dark, without city lights or aurora. EMIT has a large dynamic range, and sources 200000 times weaker than the solar-reflected signal would cause contamination commensurate with instrument noise. To prevent contamination, we create a global mask of regions on Earth that are dark at night time. We average VIIRS Day/Night Band (DNB) global mosaics over 10 months, and remove any areas within one swath width of terrain that could contain city lights. We also mask out illuminated ocean areas with nighttime fishing activity or aurora. We further subset the resulting area to remove areas in twilight where the sun is less than 20 degrees below the horizon. The remaining ocean surface is used for dark acquisitions. We ignore moonlight when scheduling dark acquisitions since the modeled signal from a full moon is below the instrument noise. Analysis of over 1000 EMIT dark acquisitions confirms this prediction, showing no measurable correlation between lunar phase and dark signal level.

The dark level naturally drifts over time with any small temperature changes in the FPA. The EMIT instrument addresses this with active cooling to hold the FPA at a stable cryogenic temperature. To assess the rate of dark current drift, we compare dark measurements on the non-sunlit side of the Earth spaced approximately 12 hours apart. The dark drift shows a bimodal distribution, with a population of pixels drifting higher and another drifting lower. The average drift is -0.16 DN over the 12 hour period, with a standard deviation of 0.67 DN. This is about an order of magnitude below other noise sources. Moreover, we typically acquire dark measurements in the same 90 minute orbit as the associated science data, rather than 12 hours apart. We conclude that the error induced by dark drift on EMIT observations is negligible.

We must also consider other faster-timescale electronic processes. *Pedestal shift* in illuminated FPAs appears as a residual error in the zero point after the dark frame is subtracted, and can differ slightly for each spectrum. We estimate this residual using several rows and columns at the periphery of the array that are blocked from external illumination. We analyze the masked rows and columns of each dark-subtracted frame, defining $d_m(c)$ to be the median of the masked rows in d_{ds} at column c.

$$d_q(r, c) = d_{ds}(r, c) - d_m(c) \tag{10}$$

Similarly, $d_n(r)$ is the median of masked rows in d_q at row r. The zero point is:

$$d_0(r, c) = d_k(r, c) + d_n(c) + d_q(r) \tag{11}$$

Subtracting d_0 from d shifts the digital number scale so that numerical zero corresponds to radiometric zero.

3.2. Bad pixel detection and repair

The next step of radiometric calibration replaces bad pixels in the FPA. We deal with two kinds of bad pixels: permanently inoperable detector elements; and elements that are unusable in the current frame because they are saturated by bright illumination. We identify permanently inoperable elements in laboratory data by flagging locations that are either (a) stuck on a single value, or (b) have a noise standard deviation which is different from the population of normal pixels. Bad pixels are easy to spot visually, since they appear as spikes in the otherwise smooth DN curves of laboratory broadband sources. A manual assessment found several additional pixels that did not trigger our statistical criterion. At the time of launch, about 120 pixels out of EMIT's 419840 were unusable, an operability rate better than 99.97%.

In addition to inoperable pixels, we also detect and replace saturated FPA elements of each frame. Bright targets such as snow at high solar elevations occasionally fill the detector well capacity. EMIT has a short integration time mode that can limit the photon flux when bright targets are anticipated. However, we rarely use this mode since it reduces radiometric sensitivity. Moreover, predicting saturation in advance is inconvenient for clouds, specular surfaces, or seasonal snow cover. Thus, it is common for images to contain a small fraction of pixels with saturated channels. We detect these channels based on their DN counts near the saturation threshold, and flag them as additional bad pixels for replacement.

Our replacement algorithm follows Chapman et al. (2019). We find a statistically appropriate replacement for each pixel based on the most similar pristine spectrum in that frame (i.e. a 1242-pixel line of image

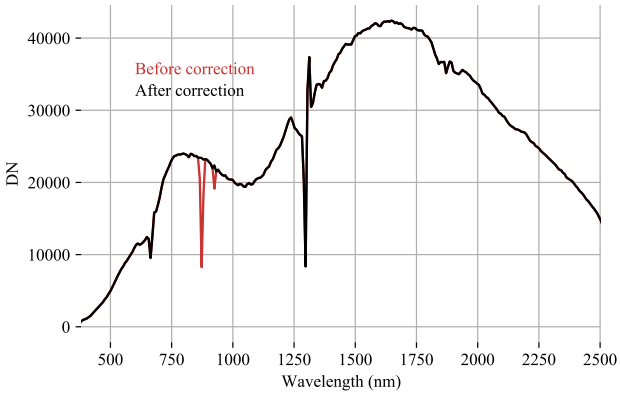

Figure 11: Procedure for replacing inoperable pixels. The spikes at 650 and 1290 nm are due to order sorting filter seams, which are correct. The spikes at 820 and 900 nm are caused by bad pixels. The replacement strategy effectively removes the artifacts.

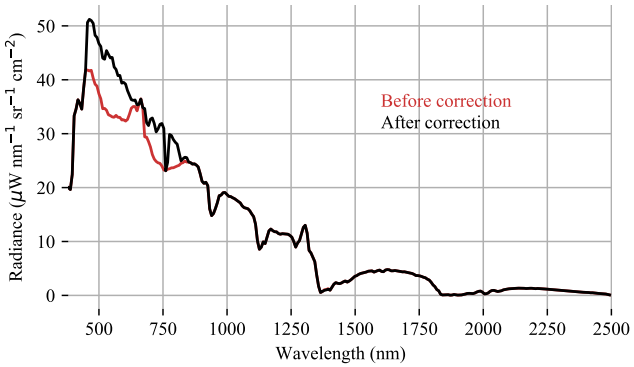

Figure 12: Procedure for replacing saturated pixels. An EMIT cloud radiance spectrum is saturated in channels brighter than about 40 μW nm^{-1} sr^{-1} cm^{-2}. The replacement values obey the statistics of cloud spectra in the same frame.

data from a single integration time). We find the most similar spectrum with a spectral angle metric (Kruse et al., 1993) and fit a linear model mapping the values from the pristine to the incomplete spectrum. We use this linear relationship to predict the missing pixels. Figure 11 applies the replacement process to a laboratory source. The replacement strategy preserves spikes at 650 and 1290 nm from the order sorting filter seams, and removes spikes at 820 and 900 nm caused by bad pixels. A manual survey of images acquired after launch determined that no additional bad pixels had appeared in the FPA, so no on-orbit update of the bad pixel map was necessary. Figure 12 shows replacement of saturated channels in a flight spectrum. We use unsaturated cloud pixels in the scene to calculate a statistically appropriate interpolant that is indistinguishable from a physical cloud spectrum. Since these values are inferred rather than measured, analysts may wish to downweight them in surface analyses. The EMIT radiance data products include a mask indicating which channels of each spectrum have been replaced.

The order sorting filter boundary at 1290 is particularly difficult to calibrate - its spectral response function and radiometric sensitivity vary across different acquisitions and substrates. However, this filter seam is "bad" for all spectra in the frame, so we cannot fix it using the Chapman et al. (2019) approach. Instead, we interpolate the radiance over the three affected channels using cubic interpolation, and mark these locations as having high uncertainty for the downstream processing. Atmospheric correction approaches capable of using this information can downweight the bad channels appropriately in the reflectance solution.

3.3. *Radiometric flat field*

The third stage of radiometric calibration transforms instrument DNs to units of radiant energy. The transformation different for every pixel on the FPA. For convenience, we decompose it into spatial and spectral dimensions: a flat field, representing spatial variability of the FPA response; and a vector of radiometric calibration coefficients, representing a channelwise translation from digital numbers to radiance units. We first measure the flat field in the laboratory by sweeping a source with constant illumination laterally across all FPA elements. We characterize the signal's rise and fall at each FPA element independently, fitting a six-degree polynomial in the time domain. The peak of this polynomial indicates the "hot spot," the maximum signal seen by the FPA element. By repeating this operation at every FPA location, we find the FPA response as if the field were spatially uniform, even though the calibration source contains spatial structure. We estimate the flat field based on the DN values in each channel, proportional to the average value of radiometric reference regions at the one and two-thirds field positions.

The flat field can change in flight over multiple spatial and temporal scales. Over short timescales, electronic drift can change the gain of each FPA element. Such changes manifest as small independent shifts in the sensitivity of different FPA elements or columns. Over long timescales, physical degradation or contamination of optical components can cause spatially-broader changes. Even sub-percent errors in relative radiometry can create visible artifacts in downstream data products. Consequently, we update the laboratory flat field in flight. Our first update aims to capture any spatially-broad changes in instrument sensitivity that had occurred since launch. We achieve this by averaging over 1600 radiance images from the first weeks of operations. We exclude from this average any pixels which fail the EMIT reflectance quality criteria due to the presence of clouds or water. We then normalize each frame of data independently by dividing out the mean spectrum. The resulting flat field update shows clear changes in visible wavelengths, but only ambiguous differences in longer wavelengths. Thus, our post-launch update only modified visible wavelengths less than 550 nm. Figure 13 shows the impact of this update on an EMIT scene over the Caspian sea. A blue band at the two thirds position disappears after the change.

Even after the post-launch flat field changes, minor column-to-column differences persist. This variability at the 0.1% level is most likely related to drift in electronic state of the detector amplifier circuits over shorter timescales. It appears visually in images as subtle vertical stripes. To capture these high spatial frequency differences we calculate updates to the flat fields for specific time segments. Early in the mission, we tried fitting a separate flat field to each image with a statistical destriping algorithm described in Chapman et al. (2019). It worked adequately for most images, and was used in the first few months of EMIT data processing. However, we soon found that very strong vertical image edges could occasionally cause errors in the flat field. To remedy this, we developed an alternative approach using longer temporal averages as in Green et al. (2011).

Our procedure considers all images in a small temporal interval around the scene to be corrected. We use a three day window for EMIT, which provides hundreds of independent images. The first step uses spatial filtering to identify homogeneous areas within each image. Specifically, we run a Sobel edge detector followed by morphological dilation to mask out areas near strong contours. This, and a

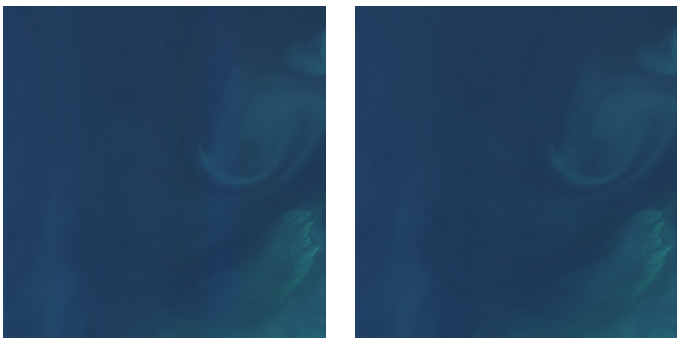

Figure 13: Caspian sea (scene ID emit20220815t042814). Left: Original EMIT image, RGB channels. Right: After post-launch flat field update.

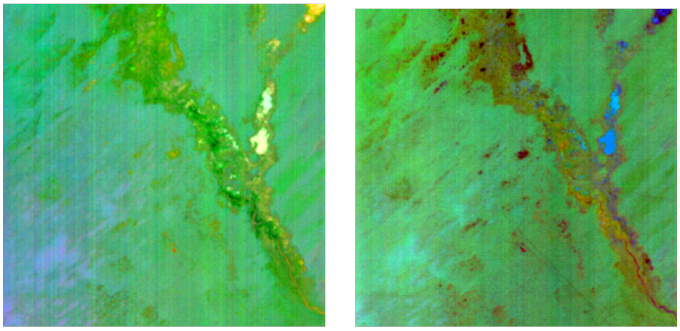

Figure 14: Arid scene (scene ID 20220828t051941). Left: Original EMIT image, MNF Bands 4-6, constrast stretched. Right: After daily flat field update. RGB color assignments are arbitrary.

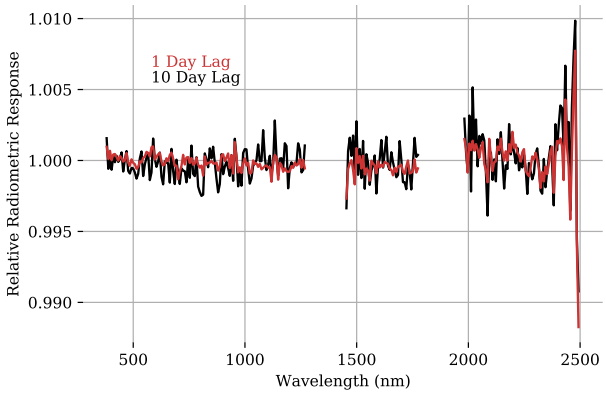

Figure 15: Example column of the flat field update showing how a single field position varies in sensitivity over one and 10 day intervals.

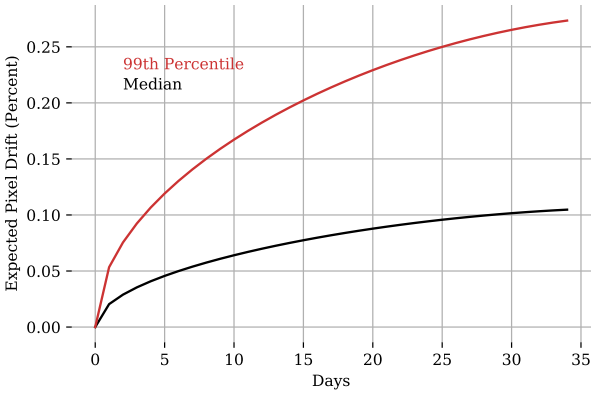

Figure 16: Flat field drift over time.

threshold to remove the brightest pixels, prevents clouds and edges in scene content from influencing the flat field. Second, we take the median of remaining pixels in the downtrack dimension as a robust estimate of the average frame for each image. Third, we filter these average frames using a high-pass spatial filter in the cross-track direction, revealing high spatial frequency variability between neighboring columns. Fourth, we create image-specific flat fields by ratioing FPA rows by the radiometric reference area of the FPA. Individual image-specific flat fields can still be influenced by measurement noise and scene content, so we combine them in a temporal median over the entire three day window for a robust estimate. For convenience, we apply this update as a multiplicative factor to each radiance image in post-processing. This approach may lead to inaccuracies, since the original flat field operation comes before optical corrections in our calibration workflow. However, the magnitude of these updates is so small (on the order of 0.1-0.3%) that any approximation error is negligible.

Figure 14 shows the effect of the flat field update on a typical EMIT image. The left panel shows three channels of a Minimum Noise Fraction (MNF) transformation, a change of basis designed to identify independent signals in the image. This representation, similar to Principal Components Analysis, tends to accentuate systematic noise and reveal vertical striping artifacts. Here, we show MNF bands 4-6, where significant vertical striping is present. The right panel shows bands 4-6 from a second MNF transformation after the updated flat field has been applied. The flat field updates improve radiometric uniformity to a level at which it should not have a major impact on EMIT's mineral mapping objectives. Figure 15 shows the magnitude of this update as a spectrum at a single field position. Flat fields compared with the difference of a single day are typically consistent to within 0.1%. After ten days, the gains have drifted a bit more, but are still generally within 0.2%. This suggests that the flat fields contain information about the average gain drift of EMIT's FPA. To quantify this drift, we fit a semivariogram to several hundred independent FPA pixels over a timespan of two months. The semivariogram quantifies the differences in any FPA element as a function of time lag. The square root of the semivariogram, plotted in Figure 16, shows the expected drift in pixel sensitivities over time. The median drift in sensitivity is approximately 0.1% over a month. However, in the same timespan, each spectrum is likely to contain channels that drift by up to 0.25%. These levels are significant enough to explain the visual striping. This underscores the value of continual flat field updates to track detector changes and ensure visual uniformity of EMIT data products.

3.4. Optical ghosts

EMIT's Dyson design creates structured stray light artifacts known colloquially as ghosts. The most significant ghost comes from an unwanted reflection from the detector that travels to the grating and back to the opposite side of the FPA. It appears as a blurred and spectrally scrambled image of the original signal. Fortunately the effect is consistent and correctable. We follow the correction approach of Zandbergen et al. (2020). We first identify the axis of symmetry ψ, the cross-track pixel location which ghosts onto itself. For each pixel at location i, the ghost spatial location j is given by $j = 2{*}\psi - i$. This allows construction of a ghost image for any scene using nearest-neighbor sampling. To find ψ, we acquire a laboratory scene with a spatially-localized source to clearly show the original and ghost features on opposite sides of the FPA. We then optimize ψ to maximize the sum of element-wise products between the ghost image pixels and the originals. The spectral structure of the ghost and original are different, but ψ should be the same for all wavelengths in a well-aligned instrument. We perform this analysis independently on each channel and use a robust median to find the axis of symmetry.

Next, we define a sparse Ghost Location Matrix (GLM) that describes the mapping of source wavelength channels to ghost channels on the opposite side of the FPA. Here, the term "channel" refers to position along the spectral dimension of the FPA. The GLM is identical at all spatial positions, so we only need to determine it once. We sweep a strong subpixel source across the EMIT wavelength range using a monochromator, and measure the channel position of the ghost reflection on the opposite side of the FPA. Figure 17 shows the resulting channel to channel mapping. Red lines show robust linear fits to each ghost order based on the RANSAC algorithm (Fischler & Bolles, 1981). Often, the signal from a single source wavelength is spread across multiple channels in the ghost reflection, so careful digital rasterization is needed.

Each channel has a different ghost magnitude based on the efficiency of the grating and the other components along its optical path. We measure these intensities with bright spatially-extended broadband sources similar to the illumination observed in flight. We illuminate just one side of the FPA so that both source and ghost can be measured independently. Several different source channels can project onto the same ghost channels. For example, in Figure 17, ghost channel 200 is a combination of reflections of four different orders coming from different wavelengths in the source spectrum. To resolve this ambiguity, we measure the stimulus and ghost spectra of over 20 different spectrally-distinct sources attenuated by different broadband filters. This collection of spectrally-diverse stimuli leads to an overdetermined system of linear equations to find the ghost reflection efficiency coefficients. To reduce the number of unknowns in this system, we manually split each linear reflection order in the GLM (i.e. the red lines in Figure 17) into piecewise linear intensity profiles. We then optimize the slope and offset of these linear intensity segments to zero out the ghost in a collection of spectrally-diverse sources. A final blurring operation, based on a concentric Gaussian operator, blurs the ghost image in spatial and spectral dimensions. This blurring operator is optimized via gradient descent to zero out the ghost feature in a spectrally-diverse training set.

To summarize, the complete ghost model consists of: the axis of symmetry; the GLM; an intensity associated with each nonzero GLM element, defined as a piecewise linear function of source channel number; and the bandwidth of the final blurring operator. After fitting these parameters, we use this description to predict the reflected ghost image for any new observed scene. We then subtract the ghost image from the original to remove the stray signal. The procedure is slightly circular in that the signal used to predict the ghost image itself contains some ghost photons. However, the ghost intensity is less than 1% of the signal, so the resulting error is vanishingly small. Figure 18 shows the result of the ghost correction procedure on a held-out laboratory source. The ghost appears as a bright stripe opposite the true source. The correction procedure erases this stripe. Figure 19 shows the associated ghost spectrum before and after the correction procedure. The ghost correction appears to work equally well in flight data; throughout the early weeks of EMIT operations, we have not found any residual ghost features in high-contrast regions.

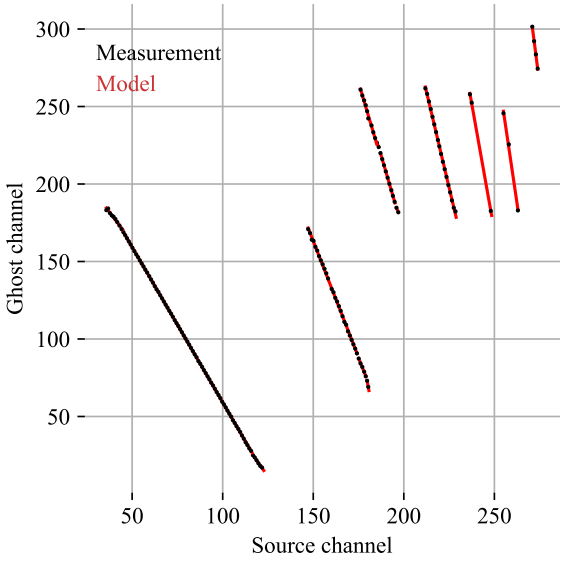

Figure 17: Ghost Location Matrix (GLM). The horizontal axis shows the original channel of the stimulus, while the vertical axis shows the position of the ghost. Often multiple source channels project onto the same ghost channel. Each channel has a different and unknown ghost intensity.

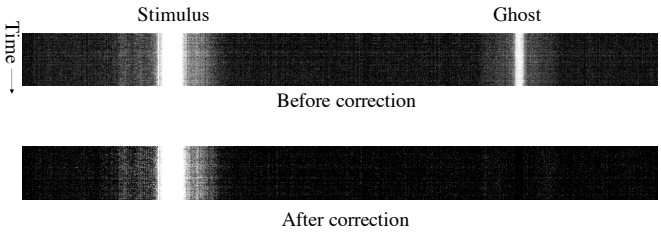

Figure 18: Ghost correction procedure. We predict the ghost associated with the measured image, and then subtract it from the original.

3.5. Radiometric calibration coefficients

The multiplicative translation from digital numbers to radiance units is stored as a vector of *Radiometric Calibration Coefficients (RCCs)*. We measure RCCs in the laboratory using a reflective panel illuminated with a source of known intensity and geometry, calculating the resulting radiance at sensor. Our calibration source is a NIST-traceable broadband lamp. The radiance prediction incorporates the known transmittance of other optical components in the chain, such as the reflectance of a fold mirror and the transmittance of a window into the vacuum chamber containing EMIT. Since much of the optical chain is outside the chamber in free air, the radiance measurement is subject to atmospheric gas absorption. The primary absorbing gas is water vapor, which has most prominent absorption shapes at 1380 and 1880 nm. We

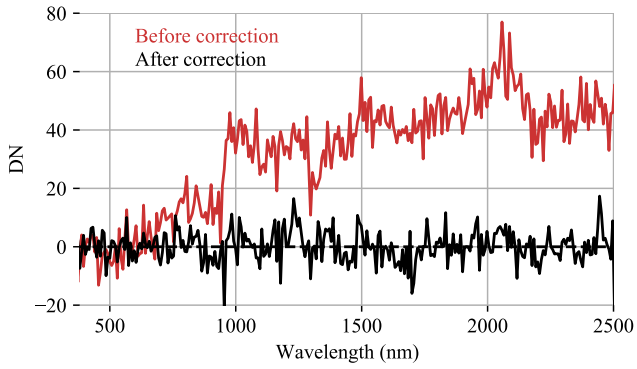

Figure 19: Ghost signal, before and after correction procedure.

address this by interpolating radiometric calibration coefficients spectrally across these water vapor absorption features.

We anticipated updating radiometric calibration coefficients in flight for several reasons. First, the instrument sensitivity can change over time as the FPA ages, and to a lesser degree between thermal cycles as the FPA accumulates trapped charge. Additionally, the instrument noise level, which is a small fraction of 1% of the signal for most targets, is always smaller than systematic errors in our laboratory calibration, so there will always be a need for refinement. Finally, the laboratory sources used for radiometric calibration have lower levels of blue and UV illumination than the sun (Helmlinger et al., 2016), so any out-of-band response in short wavelength channels can induce radiometric error when applying the calibration to flight data.

For these reasons, we adjust the radiometric calibration coefficients on-orbit using a vicarious reference target measured by a ground team with a field spectrometer. We follow the procedure outlined in Bruegge et al. (2021), which predicts the radiance at sensor and then uses the ratio with actual measurement to derive a radiometric calibration update. VSWIR imaging spectrometers are sensitive to small changes in atmospheric water vapor (Richardson et al., 2021), so reanalysis models are not sufficient. Instead, we retrieve the atmospheric aerosol and water vapor from EMIT data itself, along with the surface reflectance at the measured location, following the approach of Section 2.1. However, we now fix the instrument parameters to their calibrated values. We also retrieve pressure elevation as in Thompson et al. (2015a), by adding it to the state vector of variables that are optimized to fit the radiance spectrum. This helps obtain a more accurate Rayleigh correction, which is critical for radiometric calibration of visible wavelengths. We used data from Black Rock Playa (40.984N, 118.9675W, Figure 20), a large homogeneous playa area in Nevada, USA. The EMIT overflight took place on 18 August 2022 at approximately 21:00h UTC (scene ID emit20220818t205752). The remote measurement estimated the atmospheric water vapor content as 2.27 g cm^{-2}. Conditions were observed to be cloud free with an aerosol optical depth of 0.11 at 550 nm. Then a field team measured the same playa on 21 August at the same time of day (**??**). The field team used a leveled spectralon panel as a reflectance standard, and acquired spectra with continuous traverses across a 240x240 m area of the southwest corner of the playa. The average spectrum of the area was corrected for the absorption of the reference panel and minor offsets between detectors in the field spectrometer, and mathematically resampled to EMIT spectral characteristics. We use the remotely-measured atmospheric model to transform the in situ spectrum to a top of atmosphere radiance. The complete atmospheric description is a MODTRAN model

Figure 20: Black Rock Playa calibration site used for vicarious radiometric adjustment.

that includes estimated water vapor and aerosol values as well as all other major gases with absorption in the VSWIR spectral range, following Thompson et al. (2020). Finally, we calculate the change in radiometric calibration coefficients which would have caused the target spectrum to be measured. Uncertainties of this process include: uncertainty in the bidirectional reflectance of spectralon itself, which propagates to the in situ measurement; and inaccuracies in the atmospheric model, which could cause errors in the predicted radiance magnitude. For these reasons, we perform this adjustment in clear sky conditions and assess the update carefully with validation sites.

To validate our radiometric update, we apply the new calibration to other locations where ground truth spectra are available. We first test an in situ spectrum from the RadCalNet automated test facility at Railroad Valley, Nevada, 38.504N, 115.692W (Bouvet et al., 2019). The in situ spectrum has near perfect temporal coincidence to EMIT. We extract the EMIT data from this image location, averaging a 3x3 pixel window around the facility to mitigate the impact of single-pixel variability or spatial sampling uncertainty on the result. We then estimate its reflectance. Figure 21 shows the result; the top left panel shows the remote measurement in black, and the in situ data in red. We blank out wavelengths above 2300 nm that are not measured by the in situ spectrometer, and intervals in the shortwave infrared which are opaque due to atmospheric absorption. The bottom left plot indicates the difference, underscoring the close agreement between the remote and in situ data under optimal observing conditions. Outside the deep water absorption features at 1380 nm and 1880 nm, the mean absolute difference is just 0.7%. The largest discrepancies at short wavelengths may be residual calibration error, perhaps caused by aerosol interference during the vicarious calibration. Alternatively, it is possible they are caused by atmospheric modeling errors in the railroad valley spectrum itelf. Other departures at 1500 nm and 2100 nm may be related to uncertainty in atmospheric modeling of gaseous absorption by water vapor and CO_2.

We observed slightly larger discrepancies in a second ground-validation spectrum measured by the field team at Smith Creek, Nevada (39.326N, 117.446W, Figure 21, Right). This site was measured approximately two days earlier than the overflight, but about four hours earlier in the day, using the same protocols as Black Rock Playa (**?**). The difference in acquisition time, resulting discrepant illumination and change in the bidirectional reflectance, may account for the larger 2.2% mean absolute difference observed at this location. Nonuniformity in the playa surface might also play a part. Nevertheless, the shortwave infrared mineral features of the playa surface are well resolved in the remote data.

3.6. Instrument noise performance

We predict the EMIT instrument noise with a radiometric model. The total noise σ_{tot} is a function of scene radiance L_{obs} given in μW

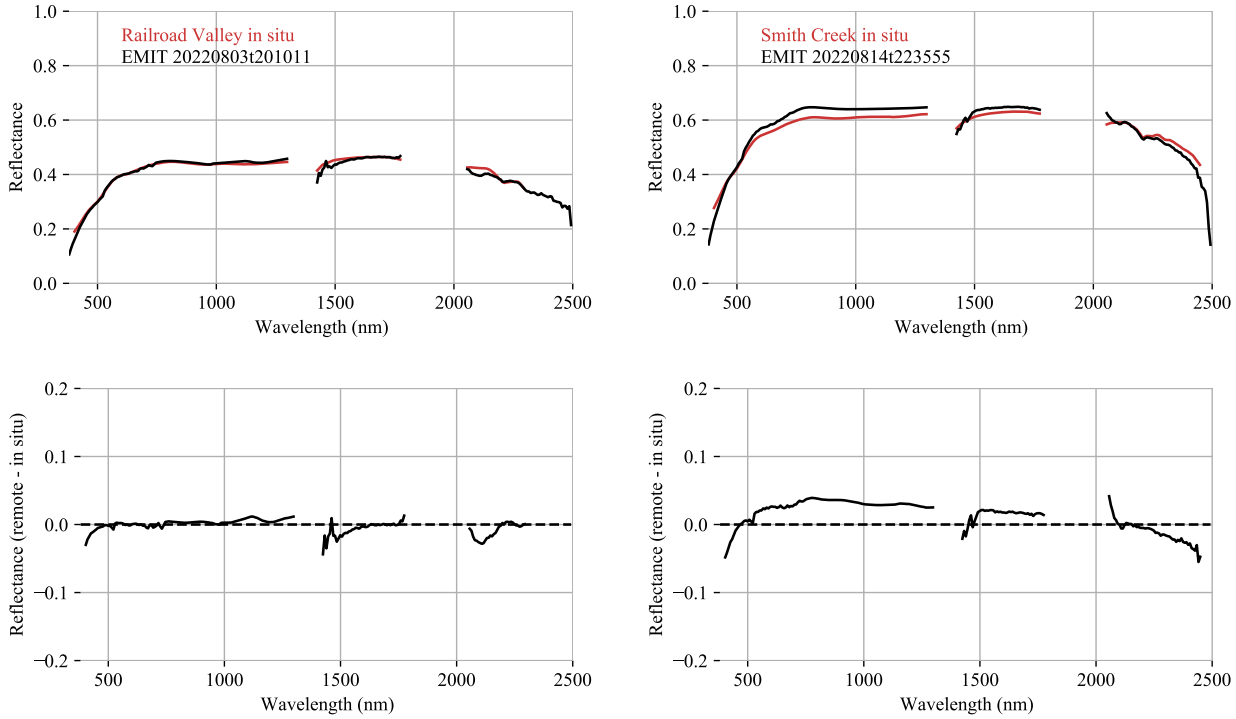

Figure 21: Reflectance comparisons of remote and in situ spectra at the Railroad Valley automated site (Left) and Smith Creek manual site (Right). The Railroad Valley spectra were nearly simultaneous, while the Smith Creek acquisitions differed in their time of day.

cm^{-2} sr^{-1} nm^{-1}.

$$\sigma_{tot} = \frac{\sqrt{\sigma_p(L_{obs})^2 + \sigma_d^2 + \sigma_q^2 + \sigma_r^2 + \sigma_e^2}}{\sqrt{2}} \tag{12}$$

Where σ_d represents dark current noise, σ_q quantization noise, σ_r read noise and σ_e electronic noise. $\sigma_p(L_{obs})$ is the photon shot noise, the standard deviation of photons arriving during the integration time. Typical EMIT spectra are the combination of two sequential integrations coadded by the FPIE-D to make a single pixel. Noise is independent over time so the coaddition reduces the noise of each spectrum by $\sqrt{2}$. The expected number of photons reaching the detector during each integration time is given by:

$$\sigma_p(L_{obs})^2 = 10^6 L_{obs} E^{-1} t_{int} \Delta_{chn} a_\omega T \tag{13}$$

with photon energy E of hc/λ Joules, where h is Planck's constant and c is the speed of light in a vacuum. The integration time is t_{int}, and the effective channel width in nanometers is Δ_{chn}. The symbol T represents the total instrument throughput, including the losses due to the grating, filters and mirrors, and the quantum efficiency. The symbol a_ω is a function of detector area a_{det}, and the instrument F number:

$$a_\omega = \frac{1}{4} a_{det} \pi F^{-2} \tag{14}$$

We form the original radiometric model from laboratory measurements of component efficiencies. on-orbit, we update the noise estimates using our on-orbit measurements of dark scenes, which suggest about 7.5 Digital Numbers (approximately 155 electrons) of noise in the absence of illumination. This is better than laboratory predictions with over 200 electrons of noise. We update the instrument transmittance T using the new vicarious radiometry, bookkeeping all changes in RCCs as changes in instrument throughput. Thus revised, the model can predict the noise experienced for new scenes.

Validating radiometric performance involves measuring noise in illuminated scenes, which is challenging due to natural variability in surface cover. Traditionally, analysts estimate instrument noise over spatially uniform playas or deserts. Over truly uniform surfaces, any differences between neighboring pixels are instrument noise (Boardman & Kruse, 2011). However, even the most homogeneous locations on Earth appear variable at EMIT's sensitivity and spatial resolution. Consequently, we need a new procedure for assessing noise. We begin with a scene that is as homogeneous as possible, and model the remaining spectral variability using a low-rank Principal Component (PC) representation. We manually select the number of components based on the eigenvalue at which an image-space projection of that coefficient degrades to spatially-decorrelated noise (Asner et al., 2012). We treat this PC projection as a de-noised image, and subtract it from the original dataset to produce an image of "noise spectra." Some of the noise leaks into the PC image and is artificially removed by this subtraction. However, instrument noise is typically isotropic and independent in each of the 285 channels, so any bias due to removing a handful of dimensions is on the order of 2% or less. We estimate measurement error using the sample covariance of this noise image. We analyze a homogeneous patch of the Caspian Sea as a dark scene dominated by read and electronic noise. This open-water scene contained three eigenvectors of scene signal. We also consider a large patch of the USGS Libya 4 calibration site (Mishra et al., 2014) as a bright scene dominated by photon shot noise. It contained six eigenvectors of scene signal.

Figure 22 shows the result. The measured noise levels lie within about 10% of the model predictions for both dark and bright scenes. The departures are largest in the darkest regions of the spectrum, such

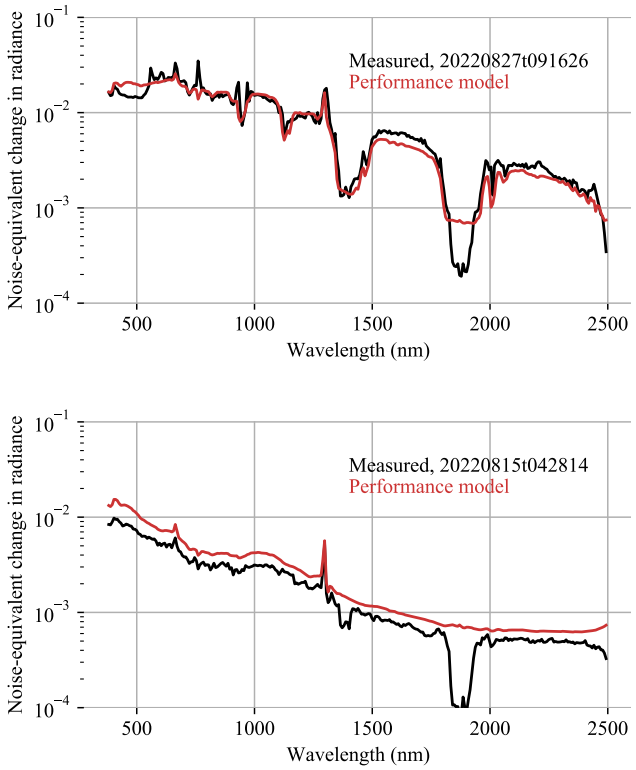

Figure 22: Top: Modeled and measured noise levels for a bright scene. Bottom: Modeled and measured noise levels for a dark scene.

as the opaque water vapor features at 1880 nm, suggesting the constant noise terms may still be too pessimistic. Figure 23 translates this noise level to an SNR for the median Libya spectrum. SNRs are above 500 in most regions of the spectrum, and above 750 in most of the visible-near infrared. The SNR is balanced across wavelengths, reflecting design decisions that allocated grating efficiency to measure features across the entire spectrum: the visible electronic transitions of iron oxides, the near infrared atmospheric features used for accurate atmospheric correction, and shortwave infrared mineral absorption features. Applying this model to EMIT's radiometric reference observation, we find SNR outperforms requirements by a factor of two (Table 1).

4. Discussion

We have completed the first on-orbit characterization of the EMIT imaging spectrometer. Table 1 summarizes our findings. EMIT's performance meets mission requirements, providing uniformity and sensitivity to enable high accuracy mineral mapping. EMIT is designed to detect small changes in mineral spectral feature depths; a change of a few percent in the depth of the hematite absorption feature, extrapolated globally, is enough to flip the sign of mineral dust radiative forcing (Li et al., 2021). EMIT's performance aims to provide statistical confidence in detecting such small changes. On-orbit, we find that performance generally meets or exceeds laboratory predictions. SNR exceeds 1000 for bright arid targets. Mean reflectance agreement better than 1% is demonstrated for coincident field data. Noise predictions match measurements to approximately 10% across diverse scene types. These results demonstrate that EMIT is ready to begin its mineral mapping mission.

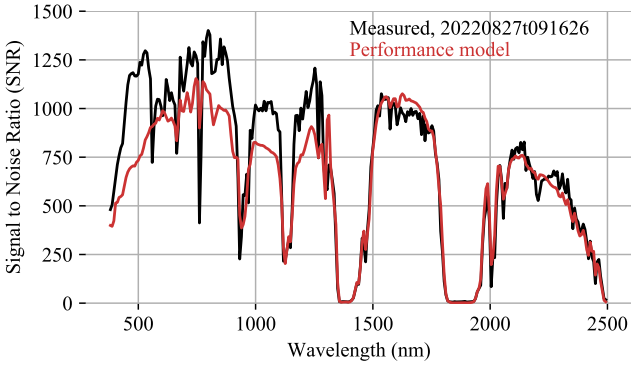

Figure 23: SNR at the Libya 4 site.

Notably, EMIT achieves this accuracy with no shutter and no onboard calibration systems of any kind. Its design philosophy emphasizes a simple optomechanical layout with high uniformity and stability to enable vicarious calibration. Accordingly, our on-orbit validation process makes extensive use of opportunistic targets in the Earth's surface and atmosphere. Imaging spectrometers are particularly suited to this strategy. Their spectral resolution can measure sharp atmospheric absorptions across the VSWIR range for spectral calibration. Spectrally-resolved surface reflectance reveals subtle distortions from poorly-modeled aerosol or cirrus that could invalidate a vicarious calibration. We use the same radiative transfer modeling tools for radiometric calibration as will be used in the final reflectance product. This ensures consistency in assumptions and minimizes the impact of any modeling errors.

Calibration is a process rather than a result. Accordingly, we will continue to track radiometric accuracy and performance over time as the mission progresses. We will use bright cloud features, the reflectance of which is well-constrained in visible wavelengths, to monitor the calibration in short wavelengths. Repeat overflights of arid regions, in particular psuedo-invariant calibration sites, can also indicate changes in relative radiometry. Cross-calibration with other on-orbit instruments can assess the absolute accuracy of these calibrations and the sensitivities to downstream products. Atmospheric fits can confirm the wavelength calibration does not change over time with inevitable instrument thermal cycles. This ensures that EMIT's mineral identification products are consistent over its lifespan.

EMIT has achieved several firsts for an instrument of its class. It has demonstrated the first on-orbit FPA alignment. Our procedure measured and then removed a micron-scale FPA tilt. This is important for mapping mineral band positions, where such nonuniformities could change geologic interpretations. The same technique could also benefit future spectrometers, such as SBG, with similarly stringent measurement needs. EMIT has also improved spectral fidelity over previous grating-based instruments, with a shallow groove design that mitigates spectral and spatial scatter. This carries benefits for both accurate atmospheric correction and mineralogy, both of which rely on sharp high contrast absorption features. Outside the uncalibrated order sorting filter seams, we have not yet been able to measure optical artifacts or infield scatter. Laboratory tests suggest they are at least three orders of magnitude below the primary signal. This underscores EMIT's potential for future science investigations beyond mineralogy. EMIT's on-orbit performance provides reason for optimism as we enter a new era of spectroscopic remote sensing of Earth's surface and atmosphere, for which this latest generation of sensors is only the vanguard.

5. Code and Data Availability

The EMIT science data system code, including the level 1b radiance calibration and associated calibration files, can be found at https://github.com/emit-sds/. Spectral libraries used in the surface/atmosphere fits are downloadable from the ECOSIS library at https://ecosis.org/package/emit-manually-adjusted-snow-and-liquids-reflectance-spectra, https://ecosis.org/package/emit-manually-adjusted-vegetation-reflectance-spectra, and https://ecosis.org/package/emit-manually-adjusted-water-reflectance-spectra.

Acknowledgment

EMIT is supported by the National Aeronautics and Space Administration Earth Venture Instrument program, under the Earth Science Division of the Science Mission Directorate. Carlos Pérez García-Pando and María Gonçalves Ageitos acknowledge support from the European Research Council (ERC) Consolidator Grant FRAGMENT (grant agreement No. 773051), and the AXA Chair on Sand and Dust Storms at the Barcelona Supercomputing Center funded by the AXA Research Fund. Martina Klose has received funding through the Helmholtz Association's Initiative and Networking Fund (grant agreement No. VH-NG-1533). This research was performed at the Jet Propulsion Laboratory, California Institute of Technology, under a contract with the National Aeronautics and Space Administration. We acknowledge the support and assistance of NASA's International Space Station Program. The USGS authors' contribution to this published Work was prepared by U.S. federal government employees as part of their official duties and constitutes a "work of the United States government," and is considered to be in the public domain and therefore domestic copyright does not apply. Any use of trade, firm, or product names is for descriptive purposes only and does not imply endorsement by the U.S. Government.

References

Alonso, K., Bachmann, M., Burch, K., Carmona, E., Cerra, D., De los Reyes, R., Dietrich, D., Heiden, U., Hölderlin, A., Ickes, J. et al. (2019). Data products, quality and validation of the dlr earth sensing imaging spectrometer (desis). *Sensors*, *19*, 4471.

Asner, G. P., Knapp, D. E., Boardman, J., Green, R. O., Kennedy-Bowdoin, T., Eastwood, M., Martin, R. E., Anderson, C., & Field, C. B. (2012). Carnegie airborne observatory-2: Increasing science data dimensionality via high-fidelity multi-sensor fusion. *Remote Sensing of Environment*, *124*, 454–465.

Berk, A., Conforti, P., Kennett, R., Perkins, T., Hawes, F., & van den Bosch, J. (2014). MODTRAN® 6: A major upgrade of the MODTRAN® radiative transfer code. *IEEE Hyperspectral Image and Signal Processing: Evolution in Remote Sensing (WHISPERS), 2014 6th Workshop on*, (pp. 1–4).

Boardman, J. W., & Kruse, F. A. (2011). Analysis of imaging spectrometer data using *n*-dimensional geometry and a mixture-tuned matched filtering approach. *IEEE Transactions on Geoscience and Remote Sensing*, *49*, 4138–4152.

Bouvet, M., Thome, K., Berthelot, B., Bialek, A., Czapla-Myers, J., Fox, N. P., Goryl, P., Henry, P., Ma, L., Marcq, S. et al. (2019). Radcalnet: A radiometric calibration network for earth observing imagers operating in the visible to shortwave infrared spectral range. *Remote Sensing*, *11*, 2401.

Brachmann, J. F., Baumgartner, A., & Lenhard, K. (2016). Calibration procedures for imaging spectrometers: improving data quality from satellite missions to uav campaigns, . *10000*, 222–233.

Bradley, C. L., Thingvold, E., Moore, L. B., Haag, J. M., Raouf, N. A., Mouroulis, P., & Green, R. O. (2020). Optical design of the earth surface mineral dust source investigation (emit) imaging spectrometer. In *Imaging Spectrometry XXIV: Applications, Sensors, and Processing* (p. 1150402). SPIE volume 11504.

Bruegge, C. J., Arnold, G. T., Czapla-Myers, J., Dominguez, R., Helmlinger, M. C., Thompson, D. R., Van den Bosch, J., & Wenny, B. N. (2021). Vicarious calibration of emas, airmspi, and aviris sensors during firex-aq. *IEEE Transactions on Geoscience and Remote Sensing*, *59*, 10286–10297.

Carmon, N., Thompson, D. R., Bohn, N., Susiluoto, J., Turmon, M., Brodrick, P. G., Connelly, D. S., Braverman, A., Cawse-Nicholson, K., Green, R. O., & Gunson, M. (2020). Uncertainty quantification for a global imaging spectroscopy surface composition investigation. *Remote Sensing of Environment*, *251*, 112038.

Cawse-Nicholson, K., Townsend, P. A., Schimel, D., Assiri, A. M., Blake, P. L., Buongiorno, M. F., Campbell, P., Carmon, N., Casey, K. A., Correa-Pabón, R. E. et al. (2021). Nasa's surface biology and geology designated observable: A perspective on surface imaging algorithms. *Remote Sensing of Environment*, *257*, 112349.

Chabrillat, S., Guanter, L., Segl, K., Foerster, S., Fischer, S., Rossner, G., Schickling, A., LaPorta, L., Honold, H.-P., & Storch, T. (2020). The enmap german spaceborne imaging spectroscopy mission: Update and highlights of recent preparatory activities. In *IGARSS 2020-2020 IEEE International Geoscience and Remote Sensing Symposium* (pp. 3278–3281). IEEE.

Chapman, J., Thompson, D. R., Helmlinger, M. C., Eastwood, M. L., Bue, B. D., Geier, S., Green, R. O., Lundeen, S. R., & Olson-Duvall, W. (2019). Spectral and Radiometric Calibration of the Next Generation Airborne Visible Infrared Spectrometer (AVIRIS-NG). *Remote Sensing*, *11*.

Cogliati, S., Sarti, F., Chiarantini, L., Cosi, M., Lorusso, R., Lopinto, E., Miglietta, F., Genesio, L., Guanter, L., Damm, A. et al. (2021). The prisma imaging spectroscopy mission: Overview and first performance analysis. *Remote Sensing of Environment*, *262*, 112499.

Connelly, D. S., Thompson, D. R., Mahowald, N. M., Li, L., Carmon, N., Okin, G. S., & Green, R. O. (2021). The emit mission information yield for mineral dust radiative forcing. *Remote Sensing of Environment*, *258*, 112380.

Cook, G. (2004). Capabilities and accommodations on the iss express pallet. In *42nd AIAA Aerospace Sciences Meeting and Exhibit* (p. 439).

Dennison, P. E., & Gardner, M. E. (2000). Hawaii 2000 vegetation species spectra. *Data set. Available on-line [http://ecosis.org] from the Ecological Spectral Information System (EcoSIS). doi:10.21232/C2HT0K*, .

Fischler, M. A., & Bolles, R. C. (1981). Random sample consensus: a paradigm for model fitting with applications to image analysis and automated cartography. *Communications of the ACM*, *24*, 381–395.

Fontenla, J., Harder, J., Livingston, W., Snow, M., & Woods, T. (2011). High-resolution solar spectral irradiance from extreme ultraviolet to far infrared. *Journal of Geophysical Research: Atmospheres*, *116*.

Gao, B.-C., Heidebrecht, K. B., & Goetz, A. F. (1993). Derivation of scaled surface reflectances from aviris data. *Remote sensing of Environment*, *44*, 165–178.

Goetz, A. F., & Srivastava, V. (1985). Mineralogical mapping in the cuprite mining district, nevada. *Proceedings of the Airborne Imaging Spectrometer (AIRS) Data Analysis Workshop: Jet Propulsion Laboratory Publication*, *85-41*, 22–29.

Green, R., Pieters, C., Mouroulis, P., Eastwood, M., Boardman, J., Glavich, T., Isaacson, P., Annadurai, M., Besse, S., Barr, D. et al. (2011). The Moon Mineralogy Mapper (M3) imaging spectrometer for lunar science: Instrument description, calibration, on-orbit measurements, science data calibration and on-orbit validation. *Journal of Geophysical Research: Planets*, *116*.

Green, R. O., Mahowald, N., Ung, C., Thompson, D. R., Bator, L., Bennet, M., Bernas, M., Blackway, N., Bradley, C., Cha, J. et al. (2020). The earth surface mineral dust source investigation: An earth science imaging spectroscopy mission. In *2020 IEEE Aerospace Conference* (pp. 1–15). IEEE.

Green, R. O., Mahowald, N. M., Clark, R. N., Ehlmann, B. L., Ginoux, P. A., Kalashnikova, O. V., Miller, R. L., Okin, G., Painter, T. H., Pérez García-Pando, C. et al. (2018). NASAś earth surface mineral dust source investigation. *AGU Fall Meeting Abstracts*, *Abstract A24D-01*.

Green, R. O. et al. (2022). EMIT mission data products. *Data available from https://lpdaac.usgs.gov/*, .

Guanter, L., Estellés, V., & Moreno, J. (2007). Spectral calibration and atmospheric correction of ultra-fine spectral and spatial resolution remote sensing data. application to casi-1500 data. *Remote Sensing of Environment*, *109*, 54–65.

Guanter, L., Kaufmann, H., Segl, K., Foerster, S., Rogass, C., Chabrillat, S., Kuester, T., Hollstein, A., Rossner, G., Chlebek, C. et al. (2015). The enmap spaceborne imaging spectroscopy mission for earth observation. *Remote*

Sensing, *7*, 8830–8857.

Helmlinger, M., Eastwood, M., Green, R., & Thompson, D. R. (2016). Solar-similar near-infra-red suppressed "blue" calibration source. In *2016 IEEE Aerospace Conference* (pp. 1–11). IEEE.

Herold, M., Roberts, D. A., Gardner, M. E., & Dennison, P. E. (2004). Spectrometry for urban area remote sensing—development and analysis of a spectral library from 350 to 2400 nm. *Remote Sensing of Environment*, *91*, 304–319. Data set available on-line [http://ecosis.org] from the Ecological Spectral Information System (EcoSIS).

Keymeulen, D., Pham, T., Klimesh, M., Allen, G., , G., Flesch, Valencia, R., Xie, H., Kiely, A., Dolman, D., Roth, K., Crocker, K., Whitlock, T., Holyoake, C., Burchfiel, S., Kampf, F., Kentley, M., Robson, A., Schepps, A., Lazaravich, B., & Stocek, D. (2022). Data compression and cloud screening using a high-performance embedded system-on-a-chip for the earth surface mineral dust source investigation (emit) imaging spectrometer on the international space station (iss). In *8th INTERNATIONAL WORKSHOP ON ON-BOARD PAYLOAD DATA COMPRESSION (OBPDC 2022)*. ESA, CNES.

Kokaly, R., Clark, R., Swayze, G., Livo, K., Hoefen, T., Pearson, N., Wise, R., Benzel, W., Lowers, H., Driscoll, R., & Klein, A. (2017). USGS Spectral Library Version 7. *U.S. Geological Survey Data*, *Series 1031*, 61.

Kruse, F. A., Lefkoff, A., Boardman, J., Heidebrecht, K., Shapiro, A., Barloon, P., & Goetz, A. (1993). The spectral image processing system (sips)—interactive visualization and analysis of imaging spectrometer data. *Remote sensing of environment*, *44*, 145–163.

Kuhlmann, G., Hueni, A., Damm, A., & Brunner, D. (2016). An algorithm for in-flight spectral calibration of imaging spectrometers. *Remote Sensing*, *8*, 1017.

Li, L., Mahowald, N. M., Miller, R. L., Pérez García-Pando, C., Klose, M., Hamilton, D. S., Gonçalves Ageitos, M., Ginoux, P., Balkanski, Y., Green, R. O. et al. (2021). Quantifying the range of the dust direct radiative effect due to source mineralogy uncertainty. *Atmospheric chemistry and physics*, *21*, 3973–4005.

Matsunaga, T., Iwasaki, A., Tachikawa, T., Tanii, J., Kashimura, O., Mouri, K., Inada, H., Tsuchida, S., Nakamura, R., Yamamoto, H. et al. (2020). Hyperspectral imager suite (hisui): its launch and current status. In *IGARSS 2020-2020 IEEE International Geoscience and Remote Sensing Symposium* (pp. 3272–3273). IEEE.

Meyer, J., Kokaly, R. F., Hoefen, T., & Cox, E. (2023a). Reflectance spectra collected august 21, at black rock desert, nevada, with an ASD© FieldSpec® 4 hi-res NG spectrometer for calibration/validation of imaging spectrometer data. *U.S. Geological Survey data release*, *https://doi.org/10.5066/P94QAHLC*.

Meyer, J., Kokaly, R. F., Hoefen, T., Cox, E., & Swayze, G. (2023b). Reflectance spectra collected august 16, at smith creek playa, nevada, with an ASD© FieldSpec® 4 hi-res NG spectrometer for calibration/validation of imaging spectrometer data. *U.S. Geological Survey data release*, *https://doi.org/10.5066/P9E2TSDF*.

Mishra, N., Helder, D., Angal, A., Choi, J., & Xiong, X. (2014). Absolute calibration of optical satellite sensors using libya 4 pseudo invariant calibration site. *Remote sensing*, *6*, 1327–1346.

Mouroulis, P., Wilson, D. W., Maker, P. D., & Muller, R. E. (1998). Convex grating types for concentric imaging spectrometers. *Applied Optics*, *37*, 7200–7208.

Nieke, J., & Rast, M. (2018). Towards the copernicus hyperspectral imaging mission for the environment (chime). In *Igarss 2018-2018 ieee international geoscience and remote sensing symposium* (pp. 157–159). IEEE.

Olson-Duvall, W., Brodrick, P., Lundeen, S., Smyth, M., & Thompson, D. R. (2022). Earth Mineral dust source InvesTigation Science Data System. *Open Source codebase at https://github.com/emit-sds*, .

Richardson, M. T., Thompson, D. R., Kurowski, M. J., & Lebsock, M. D. (2021). Boundary layer water vapour statistics from high-spatial-resolution spaceborne imaging spectroscopy. *Atmospheric Measurement Techniques*, *14*, 5555–5576.

Schläpfer, D., Borel, C. C., Keller, J., & Itten, K. I. (1998). Atmospheric precorrected differential absorption technique to retrieve columnar water vapor. *Remote Sensing of Environment*, *65*, 353–366.

Sullivan, P., Bernas, M., Liggett, E., Eastwood, M., & Green, R. (2017). Characterization of the teledyne chroma hgcdte detector for imaging spectrometers. In *2017 IEEE Aerospace Conference* (pp. 1–7). IEEE.

Thompson, D. R., Boardman, J. W., Eastwood, M. L., Green, R. O., Haag, J. M., Mouroulis, P., & Gorp, B. V. (2018a). Imaging spectrometer stray spectral response: In-flight characterization, correction, and validation. *Remote Sensing of Environment*, *204*, 850–860.

Thompson, D. R., Braverman, A., Brodrick, P. G., Candela, A., Carmon, N., Clark, R. N., Connelly, D., Green, R. O., Kokaly, R. F., Li, L. et al. (2020). Quantifying uncertainty for remote spectroscopy of surface composition. *Remote Sensing of Environment*, *247*, 111898.

Thompson, D. R., Brodrick, P. G., Cawse-Nicholson, K., Dana Chadwick, K., Green, R. O., Poulter, B., Serbin, S., Shiklomanov, A. N., Townsend, P. A., & Turpie, K. R. (2021). Spectral fidelity of earth's terrestrial and aquatic ecosystems. *Journal of Geophysical Research: Biogeosciences*, *126*, e2021JG006273.

Thompson, D. R., Cawse-Nicholson, K., Erickson, Z., Fichot, C. G., Frankenberg, C., Gao, B.-C., Gierach, M. M., Green, R. O., Jensen, D., Natraj, V., & Thompson, A. (2019a). A unified approach to estimate land and water reflectances with uncertainties for coastal imaging spectroscopy. *Remote Sensing of Environment*, *231*, 111198.

Thompson, D. R., Gao, B.-C., Green, R. O., Roberts, D. A., Dennison, P. E., & Lundeen, S. R. (2015a). Atmospheric correction for global mapping spectroscopy: Atrem advances for the hyspiri preparatory campaign. *Remote Sensing of Environment*, *167*, 64–77.

Thompson, D. R., Guanter, L., Berk, A., Gao, B.-C., Richter, R., Schl apfer, D., & Thome, K. J. (2019b). Retrieval of atmospheric parameters and surface reflectance from VSWIR imaging spectroscopy data. *Surveys in Geophysics*, *40*, 333–360.

Thompson, D. R., Leifer, I., Bovensmann, H., Eastwood, M., Fladeland, M., Frankenberg, C., Gerilowski, K., Green, R. O., Kratwurst, S., Krings, T., Luna, B., & Thorpe, A. K. (2015b). Real-time remote detection and measurement for airborne imaging spectroscopy: a case study with methane. *Atmospheric Measurement Techniques*, *8*, 4383–4397.

Thompson, D. R., Natraj, V., Green, R. O., Helmlinger, M., Gao, B.-C., & Eastwood, M. (2018b). Optimal estimation for imaging spectrometer atmospheric correction. *Remote Sensing of Environment*, *216*, 355–373.

Van Gorp, B., Mouroulis, P., Wilson, D., Green, R., Rodriguez, J., Liggett, E., & Thompson, D. (2016). Compact wide swath imaging spectrometer (CWIS): alignment and laboratory calibration. *SPIE Imaging Spectrometry XXI*, *9976*, 10–17.

Vermote, E., El Saleous, N., Justice, C., Kaufman, Y., Privette, J., Remer, L., Roger, J., & Tanre, D. (1997). Atmospheric correction of visible to middle-infrared eos-modis data over land surfaces: Background, operational algorithm and validation. *Journal of Geophysical Research: Atmospheres*, *102*, 17131–17141.

Wagner, E. P., Merz, J., & Townsend, P. A. (2018). Ecological spectral information system: an open spectral library. In *AGU Fall Meeting Abstracts* (pp. B41L–2878). volume 2018.

Zandbergen, S. R., Mouroulis, P., Small, Z., Bender, H. A., & Bellardo, J. (2020). Snow and water imaging spectrometer: final instrument characterization. In *Imaging Spectrometry XXIV: Applications, Sensors, and Processing* (pp. 27–39). SPIE volume 11504.

Zong, Y., Brown, S. W., Johnson, B. C., Lykke, K. R., & Ohno, Y. (2006). Simple spectral stray light correction method for array spectroradiometers. *Applied Optics*, *45*, 1111–1119.

List of Figures